

1 **Preparatory Slip in Laboratory Faults:**
2 **Effects of Roughness and Loading Rate**

3 **Simon Guérin-Marthe¹, Grzegorz Kwiatek¹, Lei Wang¹, Audrey Bonnelye^{1,2}, Patricia**
4 **Martínez-Garzón¹, Georg Dresen^{1,3}**

5 ¹Helmholtz Centre Potsdam, GFZ German Research Centre for Geosciences, Section 4.2:
6 Geomechanics and Scientific Drilling, Potsdam, Germany.

7 ²Free University Berlin, Berlin, Germany

8 ³University of Potsdam, Potsdam, Germany

9 Corresponding author: Simon Guérin-Marthe (simongm@gfz-potsdam.de)

10 **Key Points:**

- 11 • The spatio-temporal slip distribution during the preparatory phase of stick-slips differs
12 between rough and smooth faults.
- 13 • The average amount of preparatory slip increases with roughness and the duration of the
14 preparatory phase decreases with increasing loading rate.
- 15 • Smooth faults are more prone to instability than rough faults, and increasing loading rate
16 on rough faults promotes instability.
- 17

18 **Abstract**

19 Aseismic slip may occur during a long preparatory phase preceding earthquakes, and what controls
20 it remains poorly understood. In this study, we explored the potential dependencies of the slow
21 slip during the preparatory stage prior to stick-slip instabilities on two main factors, namely the
22 loading rate and surface roughness. To that end, we conducted shear stress-driven friction
23 experiments by imposing varying loading rates on sawcut granite samples with different surface
24 roughness at confining pressure of 35 MPa. We measured the average slip along the fault using
25 far-field displacements and strain changes, while using acoustic emission sensors and local strain
26 gages to capture local slip variations. We found that the average aseismic slip during preparatory
27 stage increases with roughness, whereas its duration decreases with increased loading rate. These
28 results also evidence a complex slip pattern on rough faults which leads to dynamic ruptures at
29 high loading rates.

30 **Plain Language Summary**

31 Earthquakes occur mostly along preexisting faults in the earth crust. These faults exhibit various
32 geometrical complexities and are subjected to different strain rates. In the laboratory, we produce
33 earthquake analogues by sliding sawcut granite blocks. We vary the geometrical complexity of the
34 faults by roughening their surfaces and modify the strain rate by displacing the blocks at varying
35 velocities. Under these different conditions, we measure how the forces accumulated by friction
36 are released, by measuring stresses and displacements applied on the block's edges, using local
37 strain deformation sensors, and by recording very small earthquakes occurring during sliding along
38 the sawcut faults. We find that smooth sawcut faults tend to release all the energy accumulated
39 very abruptly, after a very small amount of slip, regardless of the loading rate applied. The
40 processes leading to failure in the case of a rough fault are much more complex, involving a large
41 amount of slip, and numerous small earthquakes which are distributed heterogeneously in space
42 and time.

43 **1 Introduction**

44 A preparation phase preceding dynamic ruptures has been observed for a large number of
45 natural earthquakes (Bouchon et al., 2013; Durand et al., 2020; A. Kato et al., 2012; Ruiz et al.,
46 2014), and prior dynamic ruptures in the laboratory (Dresen et al., 2020; Yamashita et al., 2021).
47 At a shorter time scale, a nucleation phase can also be observed both in the field (Tape et al., 2018)
48 and in the laboratory (Latour et al., 2013). Nucleation involves accelerated slip over a finite patch
49 beyond peak stress at the rupture front (Latour et al., 2013; Rice, 1983). Previous laboratory studies
50 have revealed that the preparatory and nucleation phase prior to dynamic instability can be
51 explained by some combination of the 'cascade' and the 'preslip' models (Ellsworth & Beroza,
52 1995, McLaskey, 2019). Once a fault is close to failure, multiscale observations suggest that
53 loading of asperities due to aseismic preslip and by stress transfer between foreshocks may occur
54 concurrently (Kato & Ben-Zion, 2021; McLaskey, 2019; Yamashita et al., 2021). However, how
55 preparatory and nucleation phases are linked and what controls the spatio-temporal distribution of
56 slip during run-up to failure is still poorly understood. In addition, it remains debated in which
57 cases this preparatory phase leads to commonly observed stick-slip instabilities in the laboratory
58 where a dynamic rupture front passes through the whole contact interface.

59 Several factors have been proposed to influence the preparatory phase and the failure mode
60 of a fault, including roughness (Harbord et al., 2017; Morad et al., 2022; Okubo & Dieterich,

61 1984), loading rate (Guérin-Marthe et al., 2019; Kato et al., 1992; Marone, 1998; McLaskey &
62 Yamashita, 2017), injection rate for permeable faults (Wang et al., 2020), (effective) normal stress
63 state (Latour et al., 2013; Passelègue et al., 2020) and healing time (Marone, 1998). Looking at
64 these controlling parameters individually reveals a complex picture. Morad et al. (2022) argued
65 that an optimal roughness for triggering stick-slip instabilities on sawcut faults may exist, and
66 Harbord et al., (2017) experimentally suggested that fault stability in granite is governed by a
67 combination of roughness and normal stress almost irrespective of velocity strengthening and
68 weakening behavior. Earlier work from Ohnaka (1973) already showed that for a given roughness,
69 slip stability depends on the hardness of the two fault blocks in contact. Zhuo et al. (2022)
70 highlighted controversial findings concerning the effect of loading rate on slip. In cases, enhanced
71 loading rates were observed to promote instabilities (Guérin-Marthe et al., 2019; Kato et al., 1992;
72 McLaskey & Yamashita, 2017), while other studies suggested the opposite (Karner & Marone,
73 2000; Ohnaka, 1973). However, cumulative slip (Zhuo et al., 2022), healing times and hold periods
74 in slide-hold-slide tests (Guerin-Marthe, 2019) varied between these studies possibly affecting slip.

75 In our study, we investigate the combined influence of roughness and loading rate on the
76 stability and preparatory phase of laboratory stick-slip events in granite sawcut samples under
77 triaxial stress conditions. In particular, we focus on the spatio-temporal distribution of slip prior
78 and during instabilities using far-field mechanical data, local strain gage sensors and a dense
79 network of piezoelectric transducers.

80 **2 Materials and Methods**

81 Three cylindrical samples were prepared from La Peyratte granite with dimensions of 100 mm in
82 length and 50 mm in diameter (Young's modulus $E \approx 75$ GPa and Poisson's ratio $\nu \approx 0.25$, see
83 Figure S5). The grain size of such granite samples ranges from 0.5-1.5 mm (David et al., 1999).
84 The samples were precut at an angle $\theta=30^\circ$ to the largest stress axis direction. All sawcut surfaces
85 were precision-ground and polished using a powder composed of silicon carbide particles with a
86 diameter of 9 μm . We prepared one rough fault surface (sample R1) by sandblasting it with silicon
87 carbide particles producing a root mean square asperity height of $Z_{\text{rms}} = 14 - 16 \mu\text{m}$ and some long
88 wavelength relief. In contrast, the smooth surfaces (samples S1 & S2) are characterized by $Z_{\text{rms}} \approx$
89 3 μm (Fig. S3).

90
91 The samples were all oven-dried for at least 48 hours before mounting strain gages. Specifically,
92 two pairs of orthogonal strain gages attached to the center of two blocks (Fig. S1a-b) were used to
93 measure the elastic deformation of the rock matrix. Three additional strain gages (sgf1, sgf2 and
94 sgf3) were positioned parallel to the sawcut fault, and centered 4 mm (± 1 mm) away from it. The
95 distance between the center of two fault parallel strain gages is about 25 mm (Fig. S5). A last strain
96 gage (sgf4) was mounted normal to fault interface in the center of samples. The strain gages were
97 used to monitor local slip variations along the fault plane. After gluing strain gages, the samples
98 were placed in a rubber jacket, which is used to insulate them from the oil confining medium.

99
100 An array of 16 piezoelectric transducers surrounding the samples was used to monitor Acoustic
101 Emissions (AEs). The sensors were placed in brass housings which were glued directly on the rock
102 using epoxy, through holes pierced in the rubber jacket (Fig. S1c). The resonant frequency of these
103 sensors is 1 MHz, and the waveforms were recorded in a triggering mode at a sampling rate of 10
104 MHz. In order to locate AEs, a quasi-anisotropic velocity model composed of five horizontal layers
105 and one vertical layer was updated every ten seconds using ultrasonic pulses transmitted between

106 specific sensor pairs (Kwiatek et al., 2014, see Fig. S2 for details). The details on AE data
 107 processing including AE magnitude M_{AE} , b -value and focal mechanism estimations can be found
 108 in Text S1.

109
 110 The prepared samples were placed in a pressure vessel (Fig. S1c) and first loaded hydrostatically
 111 up to 35 MPa. The confining pressure was then maintained constant at 35 MPa in all experiments.
 112 Samples were deformed at dry conditions using a servo-controlled hydraulic Machine Testing
 113 System (MTS 4600). Axial loading was achieved by applying vertical piston displacement rates
 114 ranging from 0.05 $\mu\text{m/s}$ to 1 $\mu\text{m/s}$. A linear variable displacement transducer (LVDT) measured
 115 Δl_{LVDT} , the total displacement of the machine (with a stiffness of $K_{MTS} = 0.65 \times 10^9$ N/m or 330
 116 MPa/mm for 5 cm diameter samples) and the specimen (stiffness of 750 MPa/mm). The
 117 differential stress ($\sigma_1 - \sigma_3$) was measured using an internal load cell with a precision of ± 0.05 MPa.
 118

119 Mechanical data including differential stress, axial shortening and local strains were recorded
 120 continuously at a sampling rate of 10 Hz during the experiments. To better resolve short slip
 121 episodes, a high-speed data logging system triggered by the user also recorded with sampling rates
 122 between 2 kHz (samples S1 and R1) and 5 kHz (sample S2), during short periods of interest.
 123

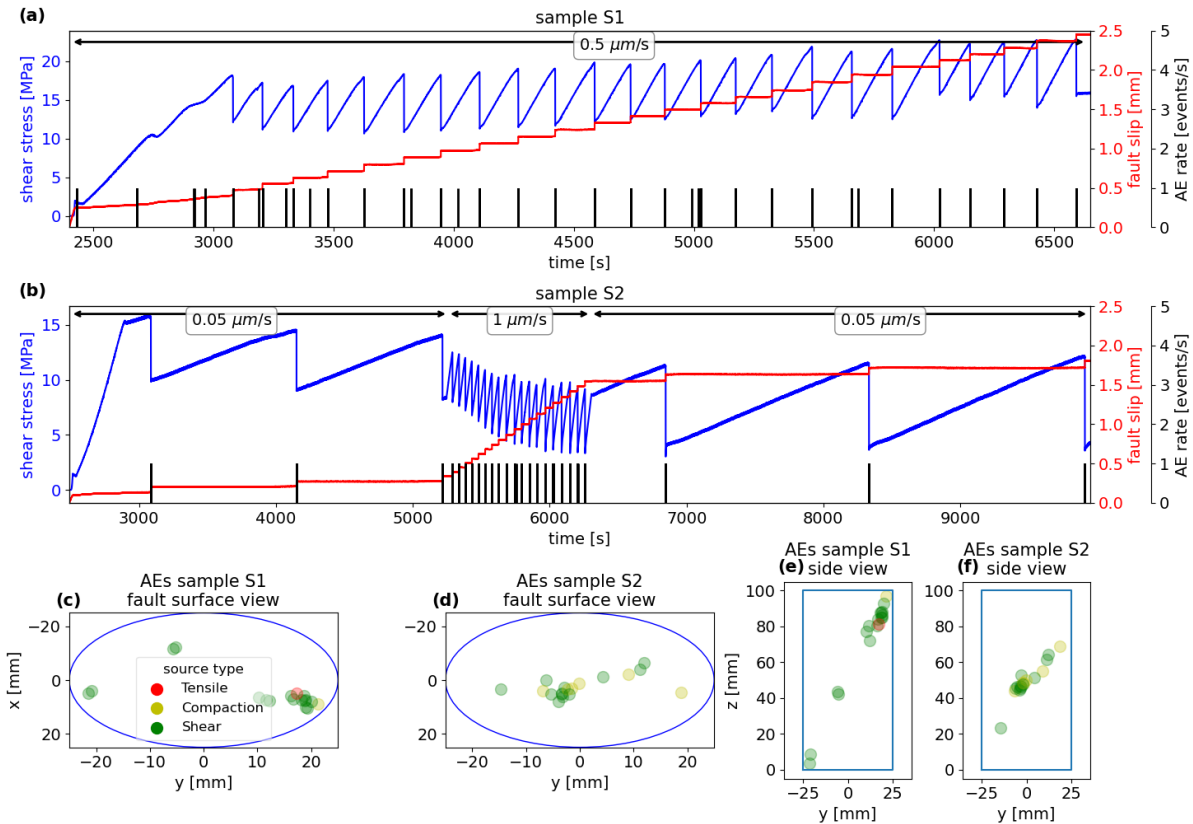
124 In triaxial loading configuration, the average shear stress τ resolved along the inclined sawcut fault
 125 plane (angle θ to the cylinder axis) was calculated from the differential stress as:

$$126 \quad 127 \quad \tau = (\sigma_1 - \sigma_3) \times \sin\theta \times \cos\theta \quad (1)$$

128
 129 and the average slip s along the fault s using:

$$130 \quad 131 \quad s = (\Delta l_{LVDT} - \Delta l_{MTS} - \Delta l_{RM}) / \cos\theta \quad (2)$$

132
 133 where Δl_{LVDT} is the total axial displacement, Δl_{MTS} is the axial shortening of the loading machine,
 134 estimated by $\Delta l_{MTS} = \text{change of the axial force} / K_{MTS}$, and Δl_{RM} is the axial deformation of rock
 135 matrix, as given by $\Delta l_{RM} = (\varepsilon_{sgv3} + \varepsilon_{sgv4}) / 2 \times L$, where $sgv3$ and $sgv4$ are vertical strain gages
 136 attached to rock matrix, and $L = 100$ mm is the sample length. Note that the stresses are also
 137 corrected for the reduction in nominal contact area between the two parts of the fault during slip.
 138 More details about the calculations can be found in Wang et al. (2020).
 139

140 **3 Results**141 **3.1 Mechanical response and AE activity**142 **3.1.1 Smooth faults**

143

144 *Figure 1: Evolution of shear stress, fault slip and AE rate on smooth faults (a) under a constant loading rate of $0.5 \mu\text{m/s}$ using*
 145 *sample S1, (b) under loading rates of $0.05 \mu\text{m/s}$ and $1 \mu\text{m/s}$ using sample S2. Acoustic emissions locations and types for (c) sample S1*
 146 *fault surface view, (d) sample S2 fault surface view, (e) sample S1 side view, (f) sample S2 side view. The source types of AE*
 147 *hypocenter can be classified into tensile, compaction and shear focal mechanism based on P-wave first motion polarities.*

148

149

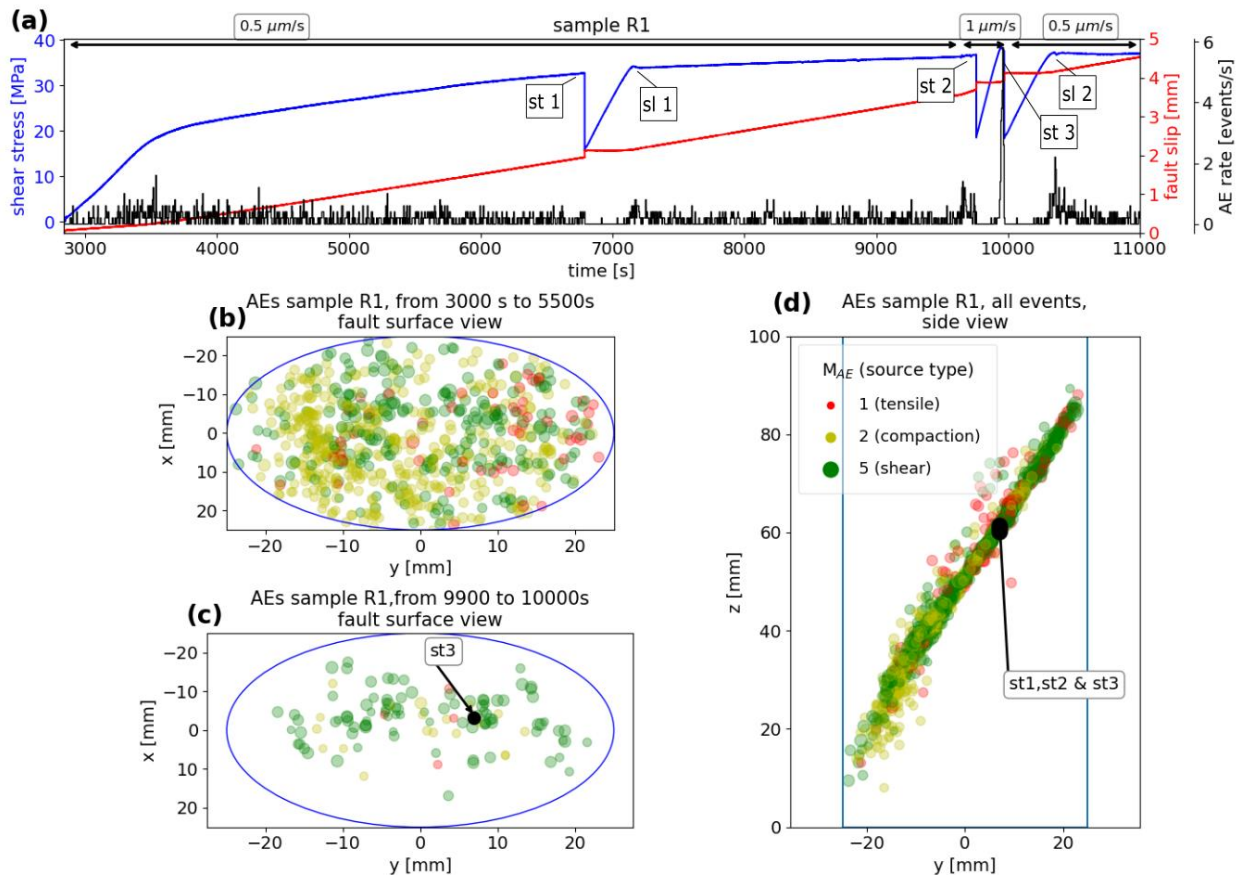
150 The two samples with smooth sawcut faults were deformed at a constant displacement rate of
 151 $0.5 \mu\text{m/s}$ and at varying displacement rates of $0.05 \mu\text{m/s}$ and $1.0 \mu\text{m/s}$, respectively (Fig. 1a, b).
 152 Both tests resulted in episodic stick-slip events with recurrence intervals decreasing from about
 153 1200 s to 60 s with loading rates increasing by a factor of 20. With progressive slip, sample S1
 154 showed a small increase in peak stress for the stick-slip events, possibly due to progressive gouge
 155 formation. The stress drop magnitude associated with the stick-slip events tends to increase with
 156 cumulative fault slip, and ranges from 5 MPa for the smallest event of sample S2 at $1 \mu\text{m/s}$ (see
 157 Fig. 1b), to 9 MPa for the largest stick-slip event on sample S1, loaded at $0.5 \mu\text{m/s}$ (see Figure 1a).
 158 In contrast, increasing loading rates from $0.05 \mu\text{m/s}$ to $1.0 \mu\text{m/s}$ showed a reduction in peak stress
 159 from 15 MPa to about 10 MPa. This was accompanied by a decrease of stress drop magnitude
 160 from 7 MPa to 5 MPa (Figure 1b).

161

162 In general, preparatory slip on smooth faults is small and failure occurs abruptly (i.e. the main slip
 163 episode lasts about 2 ms, see Fig. 4b). Additionally, we did not resolve any time delay between
 164 the different strain gage signals sampled at frequencies up to 5 kHz. Considering the spacing of
 165 2.5 cm between the strain gages (Fig. S2), and assuming a rupture front propagating in the fault
 166 plane along the fault strike direction (see Fig. S1b), this would result in rupture velocities V_r larger
 167 than 125 m/s. During the elastic loading of the locked smooth faults, we observed very little AE
 168 activity. However, every single stick-slip event was accompanied by a very large AE, and by an
 169 audible sound. Large AE events' timings correspond to the time of the main stress drop ± 100 ms,
 170 within the accuracy of the synchronized data acquisition systems. These AEs have large and
 171 typically clipped waveforms that last several milliseconds. The AE hypocenters of these large
 172 events were located on the sawcut faults partly forming localized clusters (Fig. 1c-f). Based on P-
 173 wave first motion polarities (Zang et al., 1998), the AEs display predominantly double-couple
 174 shear mechanisms.

175

3.1.2 Rough fault



176

177 *Figure 2: (a) Evolution of shear stress, fault slip and acoustic emission rate on a rough fault under loading rates of 0.5 and 1*
 178 *$\mu\text{m/s}$ using sample R1. (b) Fault surface view of corresponding AEs locations and types at the start of the experiment, before the*
 179 *first stick-slip st1. (c) AEs locations over the fault surface and their source types after the second stick-slip st2, and until stick-*
 180 *slip st3. (d) Side view of all located AEs during the experiment. The black dots indicate the location of the AEs associated with*
 181 *the main stick-slip events. Note that the size of each dot is positively correlated with the amplitude of an AE event. The source*
 182 *types of AE hypocenter can be classified into tensile, compaction and shear focal mechanism based on P-wave first motion*
 183 *polarities.*

184 Loading of the sample containing a rough fault resulted in significantly different deformation
185 compared to smooth faults. Beyond a yield stress, the sample assembly shortened by continuous
186 sliding along the sawcut fault. At a piston displacement rate of $0.5 \mu\text{m/s}$ the samples showed stable
187 sliding for about 1.5 mm and hardening with strength increasing by about 10 MPa. Sliding was
188 accompanied by prominent AE activity reaching a total 1595 events before a sudden stick-slip
189 event (st1) occurred (Fig. 2a). AEs were aligned with the sawcut fault and distributed across the
190 entire fault surface (Fig. 2b-d). Initially, during stable slip AEs were dominated by small-
191 magnitude compaction events (Fig. 2b and S9c), progressively replaced by shear events and few
192 tensile source types (cf. similar AEs microkinematic behavior for stick-slip experiments at higher
193 confining pressure in Kwiatek, Goebel, et al., 2014). The first stick-slip (st1) occurred after about
194 2 mm of stable sliding, with a stress drop of about 16 MPa, terminating the first phase of the test.
195 We note that the AE activity did not increase significantly prior to failure.

196 After event st1 the fault was locked again and elastic loading resumed to a yield point at a shear
197 stress of about 32 MPa (sl1), which is roughly similar to the peak stress reached before the stick-
198 slip event st1 occurred. Stable fault slip initiated at a peak shear stress of 34 MPa and the fault
199 strengthened again but at a smaller rate. This sliding episode lasted until the displacement rate was
200 increased to $1 \mu\text{m/s}$. Shortly after the displacement rate was increased, two stick-slips occurred
201 (st2 and st3) with stress drops of about 15-20 MPa. Both stick-slip events were preceded by bursts
202 in AE activity.

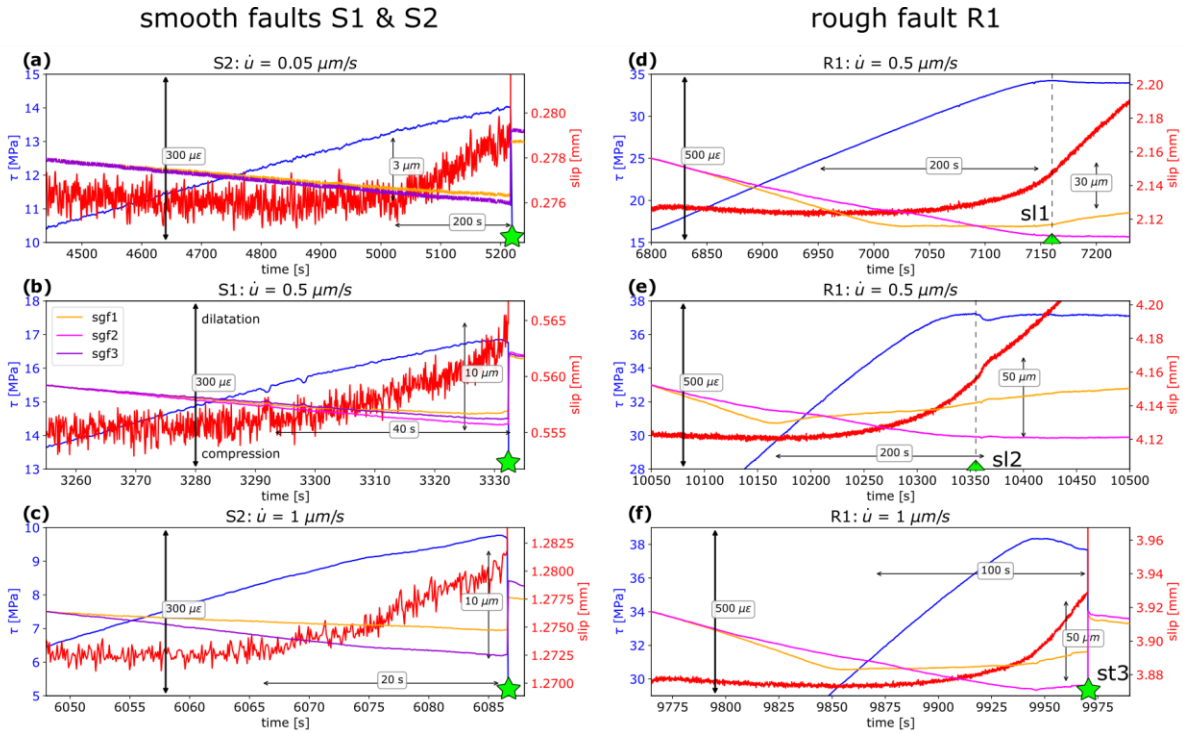
203 After the stick-slip event st3, the loading was reset to a displacement rate of $0.5 \mu\text{m/s}$. The sawcut
204 was locked and loading reached a peak stress of 38 MPa beyond which a small slow slip event
205 (sl2) initiated a third stable sliding phase. This suggests that the transition to unstable behavior at
206 the loading rate of $1 \mu\text{m/s}$ is a result of the increased loading rate rather than of the surface
207 evolution by cumulative slip. Note that slow slip sl2 is preceded by a burst of AEs similar to the
208 one preceding stick-slip event st2, showing that bursts in AEs are not necessarily followed by rapid
209 stick-slip events.

210 Overall, the located AEs align well with the fault plane (Fig. 2d). In a 100 seconds time window
211 just before stick-slip events we observed a relatively dispersed population of AEs which however
212 concentrate on local higher stress areas (Fig. 2c and S4). In general, the AE events occurring

213 shortly before stick-slip events and slow slip events display larger amplitudes and are dominantly
 214 shear focal mechanism. A few compaction events remain smaller in comparison.

215 The magnitude-frequency distribution of AEs shows a continuous trend of decreasing b -value
 216 towards the final stick slip event st3 (Fig. S9). This trend is punctuated by short episodes of rapid
 217 b -value decrease likely associated with local slip events (Dresen et al., 2020).

218 **3.2 Preparatory slip**



219
 220 *Figure 3: Evolution of shear stress (blue curve), slip (red curve) and available fault parallel strain gage signals (purple, pink and*
 221 *yellow curves), during selected phases of the rock deformation experiments. (a-c) Selected stick-slips for smooth faults S1 and S2*
 222 *at loading rates of (a) $\dot{u} = 0.05 \mu\text{m/s}$, (b) $0.5 \mu\text{m/s}$ and (c) $1 \mu\text{m/s}$. (d,e) Slow-slip events sl1 (d) and sl2 (e) at a loading rate of $\dot{u} =$*
 223 *$0.5 \mu\text{m/s}$ on the rough fault. (f) Stick-slip st3 on the rough fault R1, loaded at $\dot{u} = 1 \mu\text{m/s}$. The strain signals are offset to zero at*
 224 *the start of the plots, upwards corresponds to dilatation while downwards corresponds to compression. The strain amplitude in*
 225 *$\mu\epsilon$ is indicated on each plot. Stick-slip onsets are indicated by green stars, and slow slip onsets, corresponding to the start of*
 226 *shear stress decrease, are indicated by green triangles.*

227

228 **3.2.1 Smooth faults**

229 Here we focus on the preparatory aseismic slip prior to stick-slips on smooth sawcut faults at
 230 different background loading rates (Fig. 3a-c), showing a few representative stick-slip events in
 231 greater detail. Macroscopic slip (Eq. -2) corresponds to the average displacement between the two
 232 fault blocks. After stick-slip events, the smooth faults were locked and loading resulted in elastic
 233 deformation of the bulk sample (e.g. Fig. 3a, 4500-5000s). Beyond a yield point, slip initiated,
 234 eventually leading to failure. The total amount of fault slip for the smooth faults ($Z_{\text{rms}} \approx 3 \mu\text{m}$)
 235 during this preparatory phase is estimated to be about 3-10 μm . The duration of the preparatory

236 phase decreased with increasing loading rate, from about 200 s at 0.05 $\mu\text{m/s}$, to 40 s at 0.5 $\mu\text{m/s}$,
237 and 20 s at 1 $\mu\text{m/s}$ (Fig. 3a-c).

238

239 Within 10 s before failure (see Fig. S6a-c), we observed that the fault parallel strain gage signals
240 started diverging a few seconds before the stick-slips. At a loading rate of 0.5 $\mu\text{m/s}$, the shear stress
241 started dropping roughly one second before the slip event. At a loading rate of 1 $\mu\text{m/s}$ shear stress
242 decreased approximately 0.5 s before failure. At a low loading rate of 0.05 $\mu\text{m/s}$, this weakening
243 phase is just barely observable due to moderate mechanical noises visible on stress, slip and
244 deformation signals (Fig. S6a).

245

3.2.2 Rough faults

246 Preparatory slip before slow and fast slip events on the rough fault ($Z_{\text{rms}} \approx 14 \mu\text{m}$) showed a more
247 complex behavior (Fig. 3d-f). For example, stick-slip events st1 and st2 occurred quasi-
248 instantaneously without visible slip acceleration, irrespective of doubling the loading rate between
249 events (Fig. S6d-f). This is in contrast to stick-slip st3 and slow slip sl1 and sl2 (Fig. 3d-f). The
250 preparatory phase lasting approximately 200 s corresponds to an amount of slip up to roughly
251 50 μm (5 times the slip observed on the smooth fault at the same loading rate) for the two slow
252 slip events sl1, sl2. Prior to stick-slip st3 at a loading rate of 1 $\mu\text{m/s}$, preparatory slip duration was
253 reduced to 100 s, while the slip amount remained about 50 μm (st3, Fig. 3f). Interestingly, the start
254 of preparatory slip seems to correspond to some local slip detected on the strain signal of sgf1
255 (Fig. 3d-f), while strain gage sgf2 remains in compression.

256

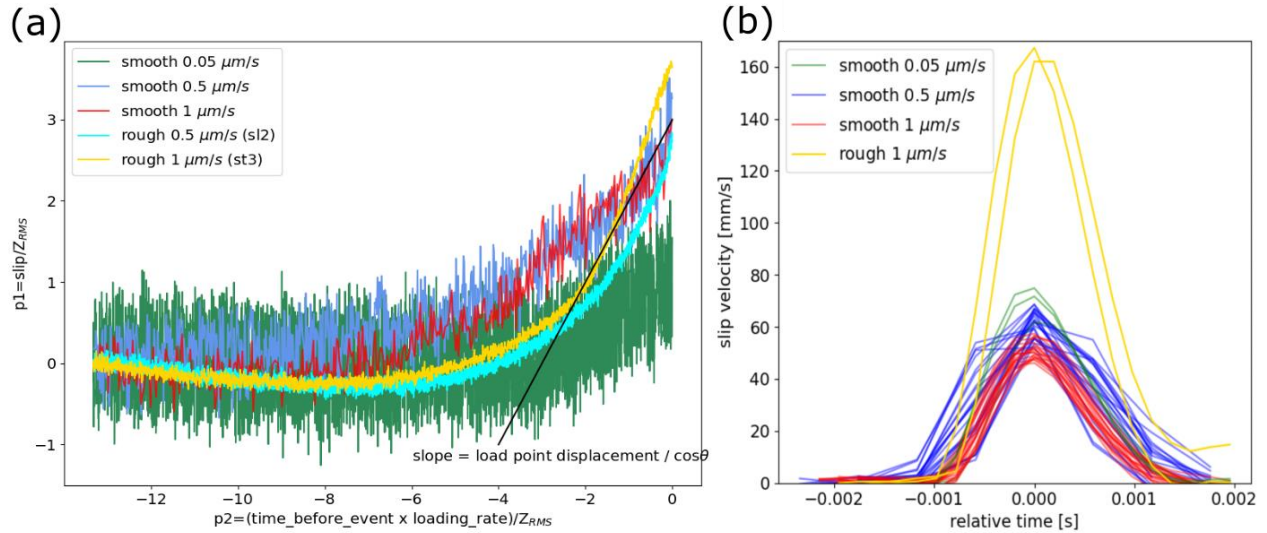
257 Prior to stick-slip st2 (Fig. S6e, f), no such preparatory slip acceleration could be observed as the
258 fault was not ‘sealed/locked’ by a previous stick-slip, but instead the fault was creeping
259 continuously. However, we observe that the increase of loading rate from 0.5 to 1 $\mu\text{m/s}$ (Fig. S6e,
260 around 9640 s), caused strong shear stress instabilities before triggering the main stick-slip.
261 Zooming in events st1 (Fig. S6d) and st2 (Fig. S6f), for which the fault continuously creeps and is
262 driven by the load point velocity (v_{lp}), we do not resolve any clear precursory signal prior to failure.
263 The precursory stress variations might be much smaller than the large stress oscillations observed
264 during a few tens of seconds preceding the events.

265

266

3.2.3 Scaling of the preparatory slip with loading rate and roughness

267



268
269
270
271
272

Figure 4: (a) Dimensionless plot of slip normalized by roughness versus the time to events (instability) normalized by loading rate and roughness (Z_{rms}). The slope corresponding to the load point displacement projected on the fault plane is indicated by a solid black line. (b) Average slip velocity between the fault blocks recorded during stick-slip events on smooth faults at loading rates of 0.05 $\mu\text{m/s}$, 0.5 $\mu\text{m/s}$ and 1 $\mu\text{m/s}$, and the rough fault at a loading rate of 1 $\mu\text{m/s}$.

273 The preparatory slip displacement depends on roughness and the duration of the preparatory slip
274 phase depends on both roughness and loading rate. To compare the data from the different tests
275 we plot the non-dimensional parameters $p1 = \text{slip}/Z_{rms}$ and $p2 = (\text{time-to-event} \times \text{loading-rate})/Z_{rms}$.
276 Although we observe that this scaling works rather well for the total normalized slip amount
277 (except for the smooth fault at the loading rate of 0.05 $\mu\text{m/s}$ where the scaled slip is approximately
278 half the slip amount observed at other loading rates), the shape of the curves for smooth and rough
279 faults are different. The slip on smooth faults increases at a low rate accounting for only a fraction
280 (10% - 30%) of the load point velocity ($0.1-0.3 v_{lp}$, see Fig. S11). For the rough fault at the loading
281 rate of 0.5 $\mu\text{m/s}$, preparatory slip clearly accelerated following the growth trend of $1/(\text{time to failure})$.
282 On the same rough fault, prior to stick-slip event st3 at the loading rate of 1 $\mu\text{m/s}$, slip
283 evolution accelerates as $1/(\text{time to failure})$ before reaching v_{lp} , and slightly exceeding it at failure
284 (see Fig. 4a and S8).

285
286
287
288

3.2.4 Slip velocity associated with the stress drop during stick-slip events

289 During the co-seismic stage of stick-slip we measured the average magnitudes of slip and stress
290 drop along the fault plane by using the recordings of axial force, displacement and deformation
291 values at the edges of samples (see Section 2). In Fig. 4b, we looked at the slip velocities during
292 the short phase where most of the slip occurs, when the high-speed data is available. For both
293 smooth and rough faults this phase lasted about 2 ms. At a loading rate of 1 $\mu\text{m/s}$, the smooth fault
294 S2 slipped with velocities between 45 to 55 mm/s, the stress drop was around 4.5 to 6 MPa and
295 the slip around 60 μm (Fig. S7). For comparison, the preparatory slip velocity on smooth faults
296 ranged from 0.005 $\mu\text{m/s}$ to 0.45 $\mu\text{m/s}$, at load point displacement rates of 0.05 $\mu\text{m/s}$ and 1 $\mu\text{m/s}$,
297 respectively. The total preparatory slip was around 10 μm , accounting for about 15% - 20% of the
298 displacement measured during stick-slip events. At a loading rate of 1 $\mu\text{m/s}$ on the rough fault, the
299 slip velocity reached 160 mm/s, the stress drop 18-19 MPa, and the slip was around 200 μm (4
300 times the amount of preparatory slip). In these experiments, the slip velocity increased with

301 decreasing loading rate, with values larger than 70 mm/s at 0.05 $\mu\text{m/s}$. Slip velocity was also
 302 strongly correlated with stress drop (Fig. S10). When plotting shear stress versus slip (Fig. S7), we
 303 obtained the fault stiffness of $K \approx 85 \text{ MPa/mm}$ for the smooth faults, and $K \approx 95 \text{ MPa/mm}$ for the
 304 rough fault.

305 **4 Discussion**

306
 307 The results of this study provide new insights into the preparatory and nucleation phase of seismic
 308 ruptures and factors controlling frictional instabilities at the laboratory scale. In particular, we
 309 stress the important role of fault roughness and loading rate for the transition to dynamic failure at
 310 elevated confining pressures. The preparatory slip phase prior to failure shows major differences
 311 between smooth and rough faults. The average fault slip, local strain variations, and the evolution
 312 of AE characteristics clearly depend on roughness. In general, our observations showed
 313 dominantly stable slip of rough faults at 35 MPa confining pressure and at load point displacement
 314 rate of 0.5 $\mu\text{m/s}$. In contrast, smooth sawcut faults produced multiple stick-slips at similar
 315 conditions. This is in good agreement with results from previous studies (e.g. Morad et al., 2022;
 316 Okubo & Dieterich, 1984).

317
 318 A plethora of studies showed that roughness of faults plays an important role in controlling fault
 319 stability (Ohnaka, 2003, Ohnaka and Shen 1999, Harbord et al., 2017; Morad et al., 2022; Okubo
 320 & Dieterich, 1984, Scholz, 1988). Okubo & Dieterich (1984) showed that the critical slip-
 321 weakening distance D_c over which the stress reaches its residual level increases with roughness.
 322 This means that the critical patch size or nucleation length required for a rupture to reach instability
 323 and accelerate to a dynamic rupture is larger for rough faults, assuming a constant stress drop.
 324 Also, the preparatory slip is expected to increase with roughness, which is in good agreement with
 325 our observations since we find that the average slip amount during the yielding phase prior to stick-
 326 slip events scales with roughness (Fig. 4a). Note that decreasing roughness does not always
 327 promote instability, as very smooth faults ($Z_{\text{rms}} < 1 \mu\text{m}$) were found to also exhibit stable behavior
 328 (Morad et al., 2022) and rough faults can become unstable at very high confining pressures
 329 (Harbord et al., 2017).

330
 331 All stick-slip events observed for smooth and rough samples were accompanied by an audible
 332 noise likely caused by the propagation of a dynamic rupture. In the framework of slip-weakening
 333 friction law, the critical nucleation length L_c for dynamic rupture has been estimated by Uenishi
 334 & Rice (2003) as:

$$335 \quad L_c = 1.158 \frac{G}{K_f} \quad (3)$$

336 where G is shear modulus and K_f is slip weakening rate (here equivalent to calculation of fault
 337 stiffness). We estimated an average value of K_f of 90 MPa/mm and $G = 30 \text{ GPa}$ for La Peyratte
 338 granite. A similar estimate for a circular patch with the critical radius R_c was given by Day (1983):
 339

$$340 \quad R_c = 7\pi/24 \frac{G}{K_f}. \quad (4)$$

341 The estimates for the critical nucleation length using Eq. 3 and Eq. 4 give 39 cm and 30 cm,
 342 respectively. Both estimates exceed the sample size suggesting that dynamic slip should not occur
 343 in stark contrast to our observations. We posit that this discrepancy may be due to the nature of
 344 the failure process. We suggest that the stress drop occurs very rapidly over a short slip distance

345 that is not captured by the data acquisition system sampling force and displacement in the far-field,
346 with maximum rates of 2 and 5 kHz, respectively. This indicates that most of the slip lasting about
347 2 ms is accommodated by frictional sliding. As discussed in Paglialunga et al., (2021), the stress
348 versus slip evolution measured likely represents a long-tail process over a slip distance that is much
349 larger than the critical slip-weakening distance D_c associated with rapid initial stress drop (by a
350 factor 50 in Paglialunga et al., 2021), and which controls rupture nucleation.

351
352 We find that recorded stick-slip duration for all events is similar (around 2 ms) as observed
353 previously in stick-slip tests performed with constant machine stiffness. This implies a linear
354 relation between slip rate (particle velocity) and stress drop (Johnson & Scholz, 1976) as also
355 suggested theoretically by Brune (1970). Our results also show that stress drop correlates with
356 maximum slip rates (Fig. S10). It explains the larger slip rates recorded on rough faults for which
357 the stress drop is also larger compared to smooth faults. This larger stress drop, although influenced
358 by the loading rate, is probably primarily controlled by the peak friction which is also larger on
359 the rough fault, in agreement with previous studies (Ohnaka, 1973).

360
361 Increasing the loading rate on rough faults (from 0.5 $\mu\text{m/s}$ to 1 $\mu\text{m/s}$) clearly promotes instability,
362 as previously observed under lower pressure conditions (Guérin-Marthe et al., 2019; Kato et al.,
363 1992; McLaskey & Yamashita, 2017). Increasing load point velocity from 0.05 $\mu\text{m/s}$ to 1 $\mu\text{m/s}$ on
364 smooth faults reduced stress drop $\Delta\tau$ of stick-slip events from 7 MPa to 5 MPa. Also, increasing
365 loading rate by a factor 20 reduces average slip rates from 70-75 mm/s to 45-55 mm/s. This
366 suggests that increasing the loading rate of smooth fault surfaces in granite does not necessarily
367 promote unstable slip. This is in contrast with the observations on rough faults. Although as
368 discussed by Guerin-Marthe (2019) instabilities could be suppressed if the contacts do not have
369 the time to re-strengthen under a sustained high loading rate, it does not seem to apply here.
370 However, as cumulative slip increases under a loading rate of 1 $\mu\text{m/s}$, the stress drops of stick-slip
371 events increased as well, suggesting rather that cumulative slip might be also influencing the
372 stability of smooth faults.

373
374 Preparatory slip on rough faults is accompanied by numerous AEs with activity increasing prior
375 to stick slip events (Fig. S8 and Fig. 3a, st2, st3). The AEs are distributed across the fault but
376 approaching failure, larger events concentrate on long wavelength fault asperities possibly
377 concentrating local stresses (Goebel et al., 2012). The AE activity preceding the failure starts when
378 an increase in slip rate is observed, in cases coinciding with macroscopic yielding or very small
379 stress drops (Dresen et al., 2020; McLaskey & Lockner, 2014, see Fig. S8). We also observe
380 diverging strain gage signals located along the faults displaying that slip is heterogeneous in space
381 and time. In general, this heterogeneity is also manifested by short episodes of significant b -value
382 fluctuations during stable slip superimposed on a general trend of decreasing b -value (Fig. S9).

383
384 From the combined mechanical data and AE characteristics of the rough fault experiment, a
385 complex slip pattern emerges. It suggests spatio-temporally distributed slip patches along the
386 surface, which are growing/coalescing with cumulative slip, while the fault blocks are
387 macroscopically slipping at the load point velocity. A large amount of slip is needed in order to
388 redistribute stresses (by breaking asperities) and create a critical slip patch causing instability. The
389 coalescence of slipping patches would agree with the acceleration of preparatory slip with time
390 observed for the rough faults when they are previously locked. This could also help explaining the

391 loading rate role in promoting instabilities at 1 $\mu\text{m/s}$. Indeed, under a low loading rate, if enough
392 asperities are able to re-strengthen, while others are broken, then the fault can slip continuously in
393 a stable fashion. However, as the re-strengthening of contacts is not only slip-dependent, but also
394 time-dependent (Dieterich & Kilgore, 1994), increasing loading rate could also rise the proportion
395 of weak/broken versus strong contacts, and therefore increases the likelihood of having a large
396 slipping patch close to the critical size for dynamic rupture.

397
398 On smooth faults, the behavior is different. First, almost no AEs are detected during the preparatory
399 phase, from the onset of yielding until the stick-slip. This is a possible effect of the small elevation
400 of contacts which upon breaking do not necessarily trigger AEs above the noise level, and is
401 generally comparable to what has been observed for stick-slip experiment on smooth faults in
402 Kwiatek, Goebel, et al. (2014). Then, we observe that smooth faults are always unstable with
403 regular stick-slip events, for the whole range of load point velocities applied (0.05-1 $\mu\text{m/s}$). We
404 argue that on smooth faults, once a slipping patch or crack has formed, the stress increase at its
405 tips might be sufficient to break the small contacts immediately surrounding it. A slipping zone
406 could therefore expand and accelerate relatively easily, reaching dynamic rupture velocities. In
407 comparison, if an asperity breaks or a patch starts slipping on a rough fault, there might be strong
408 contacts preventing further growth, and the next asperity to break might not be an adjacent one.
409 As long as the slipping patches are not able to merge reaching the critical length for instability, we
410 might expect stable sliding.

411 **Conflict of Interest**

412
413 The authors declare no conflicts of interest relevant to this study.

414 **Data Availability Statement**

415
416 The data used in this manuscript are available online (<https://doi.org/10.5281/zenodo.6411819>).

417 **Acknowledgments**

418
419 S.G-M and P.M.G. acknowledge funding from the Helmholtz Association in the frame of the
420 Young Investigators Group VH-NG-1232 (SAIDAN). The authors would also like to thank
421 Michael Naumann and Stefan Gehrman for the technical help, and Laboratoire Colas Centre
422 Ouest for providing the La Peyratte granite samples.

423 **References**

- 424
425
426
427
428
429 Bouchon, M., Durand, V., Marsan, D., Karabulut, H., & Schmittbuhl, J. (2013). The long
430 precursory phase of most large interplate earthquakes. *Nature Geoscience*, 6(4), 299–
431 302. <https://doi.org/10.1038/ngeo1770>
432 Brune J.N. (1970). Tectonic stress and the spectra of seismic shear waves from earthquakes.
433 *J Geophys Res*, 75(26). <https://doi.org/10.1029/jb075i026p04997>
434 David, C., Menéndez, B., & Darot, M. (1999). Influence of stress-induced and thermal
435 cracking on physical properties and microstructure of La Peyratte granite.

- 436 *International Journal of Rock Mechanics and Mining Sciences*, 36(4).
 437 [https://doi.org/10.1016/S0148-9062\(99\)00010-8](https://doi.org/10.1016/S0148-9062(99)00010-8)
- 438 Day, S. M. (1983). Three-dimensional simulation of spontaneous rupture: The effect of
 439 nonuniform prestress. *International Journal of Rock Mechanics and Mining Sciences*
 440 & *Geomechanics Abstracts*, 20(5). [https://doi.org/10.1016/0148-9062\(83\)90099-2](https://doi.org/10.1016/0148-9062(83)90099-2)
- 441 Dieterich, J. H., & Kilgore, B. D. (1994). Direct observation of frictional contacts: New
 442 insights for state-dependent properties. *Pure and Applied Geophysics PAGEOPH*,
 443 143(1–3). <https://doi.org/10.1007/BF00874332>
- 444 Dresen, G., Kwiatek, G., Goebel, T., & Ben-Zion, Y. (2020). Seismic and Aseismic
 445 Preparatory Processes Before Large Stick–Slip Failure. *Pure and Applied Geophysics*,
 446 177(12), 5741–5760. <https://doi.org/10.1007/s00024-020-02605-x>
- 447 Durand, V., Bentz, S., Kwiatek, G., Dresen, G., Wollin, C., Heidbach, O., et al. (2020). A
 448 two-scale preparation phase preceded an Mw 5.8 earthquake in the Sea of Marmara
 449 Offshore Istanbul, Turkey. *Seismological Research Letters*, 91(6), 3139–3147.
 450 <https://doi.org/10.1785/0220200110>
- 451 Ellsworth, W. L., & Beroza, G. C. (1995). Seismic Evidence for an Earthquake Nucleation
 452 Phase. *Science*. <https://doi.org/10.1126/science.268.5212.851>
- 453 Font, Y., Kao, H., Lallemand, S., Liu, C. S., & Chiao, L. Y. (2004). Hypocentre
 454 determination offshore of eastern Taiwan using the maximum intersection method.
 455 *Geophysical Journal International*, 158(2). <https://doi.org/10.1111/j.1365-246X.2004.02317.x>
- 457 Goebel, T. H. W., Becker, T. W., Schorlemmer, D., Stanchits, S., Sammis, C., Rybacki, E.,
 458 & Dresen, G. (2012). Identifying fault heterogeneity through mapping spatial
 459 anomalies in acoustic emission statistics. *Journal of Geophysical Research: Solid*
 460 *Earth*, 117(3). <https://doi.org/10.1029/2011JB008763>
- 461 Guerin-Marthe, S. (2019). Analogue and numerical models of earthquake rupture, *Chapter*
 462 *5*, 218. Retrieved from <http://theses.dur.ac.uk/13341/>
- 463 Guérin-Marthe, S., Nielsen, S., Bird, R., Giani, S., & di Toro, G. (2019). Earthquake
 464 Nucleation Size: Evidence of Loading Rate Dependence in Laboratory Faults. *Journal*
 465 *of Geophysical Research: Solid Earth*, 124(1). <https://doi.org/10.1029/2018JB016803>
- 466 Guo, Z., & Ogata, Y. (1997). Statistical relations between the parameters of aftershocks in
 467 time, space, and magnitude. *Journal of Geophysical Research: Solid Earth*, 102(B2).
 468 <https://doi.org/10.1029/96jb02946>
- 469 Harbord, C. W. A., Nielsen, S. B., de Paola, N., & Holdsworth, R. E. (2017). Earthquake
 470 nucleation on rough faults. *Geology*, 45(10), 931–934.
 471 <https://doi.org/10.1130/G39181.1>
- 472 Johnson, T. L., & Scholz, C. H. (1976). Dynamic properties of stick-slip friction of rock.
 473 *Journal of Geophysical Research*, 81(5). <https://doi.org/10.1029/jb081i005p00881>
- 474 Karner, S. L., & Marone, C. (2000). Effects of loading rate and normal stress on stress drop
 475 and stick-slip recurrence interval. In *Geophysical Monograph Series* (Vol. 120).
 476 <https://doi.org/10.1029/GM120p0187>
- 477 Kato, A., & Ben-Zion, Y. (2021). The generation of large earthquakes. *Nature Reviews*
 478 *Earth & Environment*, 2(1), 26–39. <https://doi.org/10.1038/s43017-020-00108-w>
- 479 Kato, A., Obara, K., Igarashi, T., Tsuruoka, H., Nakagawa, S., & Hirata, N. (2012).
 480 Propagation of slow slip leading up to the 2011 Mw 9.0 Tohoku-Oki earthquake.
 481 *Science*, 335(6069). <https://doi.org/10.1126/science.1215141>

- 482 Kato, N., Yamamoto, K., Yamamoto, H., Hirasawa, T., Aki, K., Ohnaka, M., et al. (1992).
483 *Strain-rate effect on frictional strength and the slip nucleation process.*
- 484 Kwiatek, G., Charalampidou, E. M., Dresen, G., & Stanchits, S. (2014). An improved
485 method for seismic moment tensor inversion of acoustic emissions through assessment
486 of sensor coupling and sensitivity to incidence angle. *International Journal of Rock*
487 *Mechanics and Mining Sciences*, 65. <https://doi.org/10.1016/j.ijrmmms.2013.11.005>
- 488 Kwiatek, G., Goebel, T. H. W., & Dresen, G. (2014). Seismic moment tensor and b value
489 variations over successive seismic cycles in laboratory stick-slip experiments.
490 *Geophysical Research Letters*, 41(16). <https://doi.org/10.1002/2014GL060159>
- 491 Latour, S., Schubnel, A., Nielsen, S., Madariaga, R., & Vinciguerra, S. (2013).
492 Characterization of nucleation during laboratory earthquakes. *Geophysical Research*
493 *Letters*, 40(19). <https://doi.org/10.1002/grl.50974>
- 494 Marone, C. (1998). The effect of loading rate on static friction and the rate of fault healing
495 during the earthquake cycle. *Nature*, 69–72.
- 496 McLaskey, G. C. (2019). Earthquake Initiation From Laboratory Observations and
497 Implications for Foreshocks. *Journal of Geophysical Research: Solid Earth*, 124(12).
498 <https://doi.org/10.1029/2019JB018363>
- 499 McLaskey, G. C., & Lockner, D. A. (2014). Preslip and cascade processes initiating
500 laboratory stick slip. *Journal of Geophysical Research: Solid Earth*, 119(8).
501 <https://doi.org/10.1002/2014JB011220>
- 502 Mclasley, G. C., & Yamashita, F. (2017). Slow and fast ruptures on a laboratory fault
503 controlled by loading characteristics. *Journal of Geophysical Research: Solid Earth*,
504 122(5), 3719–3738. <https://doi.org/10.1002/2016JB013681>
- 505 Morad, D., Sagy, A., Tal, Y., & Hatzor, Y. H. (2022). Fault roughness controls sliding
506 instability. *Earth and Planetary Science Letters*, 579.
507 <https://doi.org/10.1016/j.epsl.2022.117365>
- 508 Nelder, J. A., & Mead, R. (1965). A Simplex Method for Function Minimization. *The*
509 *Computer Journal*, 7(4). <https://doi.org/10.1093/comjnl/7.4.308>
- 510 Ohnaka, M. (1973). Experimental studies of stick-slip and their application to the
511 earthquake source mechanism. *Journal of Physics of the Earth*, 21(3).
512 <https://doi.org/10.4294/jpe1952.21.285>
- 513 Okubo, P. G., & Dieterich, J. H. (1984). Effects of physical fault properties on frictional
514 instabilities produced on simulated faults. *Journal of Geophysical Research*, 89(B7),
515 5817–5827. <https://doi.org/10.1029/JB089iB07p05817>
- 516 Paglialunga, F., Passelègue, F., Brantut, N., Barras, F., Lebihain, M., & Violay, M. (2021).
517 On the scale dependence in the dynamics of frictional rupture: constant fracture energy
518 versus size-dependent breakdown work.
- 519 Passelègue, F. X., Almakari, M., Dublanchet, P., Barras, F., Fortin, J., & Violay, M. (2020).
520 Initial effective stress controls the nature of earthquakes. *Nature Communications*,
521 11(1). <https://doi.org/10.1038/s41467-020-18937-0>
- 522 Rice, J. R. (1983). Constitutive relations for fault slip and earthquake instabilities. *Pure and*
523 *Applied Geophysics PAGEOPH*, 121(3). <https://doi.org/10.1007/BF02590151>
- 524 Ross, Z. E., Meier, M. A., & Hauksson, E. (2018). P Wave Arrival Picking and First-
525 Motion Polarity Determination With Deep Learning. *Journal of Geophysical*
526 *Research: Solid Earth*, 123(6). <https://doi.org/10.1029/2017JB015251>

- 527 Ruiz, S., Metois, M., Fuenzalida, A., Ruiz, J., Leyton, F., Grandin, R., et al. (2014). Intense
528 foreshocks and a slow slip event preceded the 2014 Iquique Mw8.1 earthquake.
529 *Science*, (6201), 1165–1169. <https://doi.org/10.1126/science.1256074>
- 530 Shi, Y., & Bolt, B. A. (1982). The standard error of the magnitude-frequency b value .
531 *Bulletin of the Seismological Society of America*, 72(5).
532 <https://doi.org/10.1785/bssa0720051677>
- 533 Stanchits, S., Mayr, S., Shapiro, S., & Dresen, G. (2011). Fracturing of porous rock induced
534 by fluid injection. *Tectonophysics*, 503(1–2).
535 <https://doi.org/10.1016/j.tecto.2010.09.022>
- 536 Tape, C., Holtkamp, S., Silwal, V., Hawthorne, J., Kaneko, Y., Ampuero, J. P., et al. (2018).
537 Earthquake nucleation and fault slip complexity in the lower crust of central Alaska.
538 *Nature Geoscience*, 11(7). <https://doi.org/10.1038/s41561-018-0144-2>
- 539 Uenishi, K., & Rice, J. R. (2003). Universal nucleation length for slip-weakening rupture
540 instability under nonuniform fault loading. *Journal of Geophysical Research: Solid*
541 *Earth*, 108(B1). <https://doi.org/10.1029/2001JB001681>
- 542 Wang, L., Kwiatek, G., Rybacki, E., Bonnelye, A., Bohnhoff, M., & Dresen, G. (2020).
543 Laboratory Study on Fluid-Induced Fault Slip Behavior: The Role of Fluid
544 Pressurization Rate. *Geophysical Research Letters*, 47(6).
545 <https://doi.org/10.1029/2019GL086627>
- 546 Yamashita, F., Fukuyama, E., Xu, S., Kawakata, H., Mizoguchi, K., & Takizawa, S. (2021).
547 Two end-member earthquake preparations illuminated by foreshock activity on a
548 meter-scale laboratory fault. *Nature Communications*, 12(1).
549 <https://doi.org/10.1038/s41467-021-24625-4>
- 550 Zang, A., Wagner, F. C., Stanchits, S., Dresen, G., Andresen, R., & Haidekker, M. A.
551 (1998). Source analysis of acoustic emissions in Aue granite cores under symmetric
552 and asymmetric compressive loads. *Geophysical Journal International*, 135(3).
553 <https://doi.org/10.1046/j.1365-246X.1998.00706.x>
- 554 Zhuo, Y.-Q., Liu, P., Guo, Y., Chen, H., Chen, S., & Wang, K. (2022). Cross-effects of
555 loading rate and cumulative fault slip on pre-seismic rupture and unstable slip rate of
556 laboratory earthquakes. *Tectonophysics*, 826, 229266.
557 <https://doi.org/10.1016/j.tecto.2022.229266>
- 558